Results in Engineering 27 (2025) 106062

Contents lists available at ScienceDirect

Results in Engineering

journal homepage: www.sciencedirect.com/journal/results-in-engineering

Numerical simulation of laminar and two-phase flow and heat transfer of water-aluminum oxide nanofluid in microchannel with V-shaped ribs

Ali Koveiti [a], Ali B.M. Ali [b], Sabah F.H. Alhamdi [c], Omid Ali Akbari [d,*], Gholamreza Ahmadi [e], Soheil Salahshour [f,g,h], Sh. Baghaei [i,*]

[a] Department of Mechanical Engineering, Khomeinishahr Branch, Islamic Azad University, Khomeinishahr, Iran
[b] Air Conditioning Engineering Department, College of Engineering, University of Warith Al-Anbiyaa, Karbala, Iraq
[c] Department of Mechanical Engineering, University of Misan, Amarah, Misan 62001, Iraq
[d] Department of Mechanical Engineering, Faculty of Engineering, Arak University, Arak 38156-88349, Iran
[e] Faculty of Mechanical and Energy Engineering, Shahid Beheshti University, Tehran, Iran
[f] Faculty of Engineering and Natural Sciences, Istanbul Okan University, Istanbul, Turkey
[g] Faculty of Engineering and Natural Sciences, Bahcesehir University, Istanbul, Turkey
[h] Research Center of Applied Mathematics, Khazar University, Baku, Azerbaijan
[i] Fast Computing Center, Shabihsazan Ati Pars, Tehran, Iran

ARTICLE INFO

Keywords:
Rectangular microchannel
Combined convection heat transfer
Volume fraction
Nanofluid
V-shaped rib

ABSTRACT

In this study, a rectangular microchannel equipped with V-shaped ribs at the bottom filled with a solid-liquid suspension of water-aluminum oxide is evaluated. To better estimate the movement of solid-liquid phases, the two-phase mixture method simulates the incompressible water-aluminum oxide nanofluid (NF). The results are obtained for different hydrodynamic and heat transfer values and volume fraction of solid nanoparticles (φ) = 0, 2, and 4 % and Reynolds number (Re) = 400-1200. The finite volume method (FVM) in three-dimensional (3D) space is used for simulations. The results show that the fluid in the areas after the ribs has reverse velocity gradients and by increasing α, the wake area increases. By increasing α, the vortices and velocity gradients separated from the ribs' surfaces penetrate the central core of the flow. At $\alpha = 50^{\circ}$, because the fluid collides with the ribs, it is associated with a greater velocity drop and the creation of stronger vortices, so C_f has the highest value. In the ribbed region and for $\alpha = 40^{\circ}$ to $\alpha = 50^{\circ}$, the changes in local Nusselt number are similar. By increasing φ, the penetration of fluid to the back of the ribs becomes possible; In these diagrams, the minimum amount of S_{gen} is for $\alpha = 40^{\circ}$ and 50°. In general, the behavior of S_{gen} is the same as the growth of dimensionless temperature, and at Re= 400, the maximum amount of S_{gen} is related to $\alpha = 20^{\circ}$.

1. Introduction

Improving the properties of conventional fluids by strengthening the thermal conductivity coefficient in nanofluids (NFs) will be promising for their use in different industries such as power stations, petrochemicals, pharmaceuticals, automobiles, electronics, etc., as a good heat transfer fluid. The reason for the use of NFs in industrial and practical applications is the development of effective heat transfer characteristics in them. For this purpose, nowadays many studies have been conducted by researchers focusing on heat transfer using NFs in smooth and rough geometries and different dimensions [1,2]. Moreover, vortex generators are a suitable tool to increase heat transfer in various heat exchangers and improve flow mixing in the pharmaceutical, medical, and petrochemical industries [3]. In their numerical study, Bahiraei et al. [4] evaluated the effects of increasing heat transfer by simultaneously using V-shaped fins and NF inside a 3D square channel. Using the two-phase mixture method, they studied the entropy behavior in the water/-copper NF flow in φ = 0.01-0.03. In their numerical study, they evaluated the effect of the structure of V-shaped ribs with changes in the rib pitch and its height (three rib pitches and three different heights). They used the finite volume method (FVM) and SIMPLE algorithm. The results showed that increasing φ decreases the total entropy generation ($S_{gen,tot}$). They showed that for the nanoparticle with φ = 0.03 and a 5 mm V-shaped rib, $S_{gen,tot}$ is about 31.85 %. At the same time, using a longer rib and a smaller pitch (simultaneously) increases the effectiveness of the second law of thermodynamics. Kerdarian and Kianpour [5] investigated the behavior of water-copper NF in a nanochannel consisting of

* Corresponding authors.
E-mail addresses: cfd.eng.omid@gmail.com (O.A. Akbari), shaghaieghbaghaie@yahoo.com (Sh. Baghaei).

https://doi.org/10.1016/j.rineng.2025.106062
Received 21 April 2025; Received in revised form 17 May 2025; Accepted 1 July 2025
Available online 4 July 2025

Nomenclatures

A	Area, m^2
C_f	Poisier number
C_p	Specific heat, J/kg.K
d	Rib thickness, m (in Fig. 2) and Molecular diameter, nm (in Eq. (11))
f	Friction factor
FVM	Finite volume method
H	Height of the microchannel, nm
k	Conduction heat transfer coefficient, W/m.K
L	Length, m
Nu	Nusselt number
P	Perimeter of the shape, m
P	Pressure, Pa
PEC	Thermal-fluid efficiency
P_P	Pumping power, W
Pr	Parandtle number
q''	Heat flux, W/m^2
Re	Reynolds number
S_{gen}	Entropy generation
T	Temperature, K
U, V, W	Dimensionless velocity components in the x,y, and z directions
u, v, w	Velocity components in the x, y, and z directions
X, Y, Z	Dimensionless lines of length, width, and height

Greek signs

ρ	Density, kg/m^3
μ	Viscosity, Pa.s
A	Heat penetration, m^2/s
β	Volume expansion coefficient, k^{-1}
φ	The volume fraction of solid particles
α	Attack angle(°)

Subtitle

f	Liquid
S	Solid particles
S	Smooth
NF	Nanofluid
ave	Average

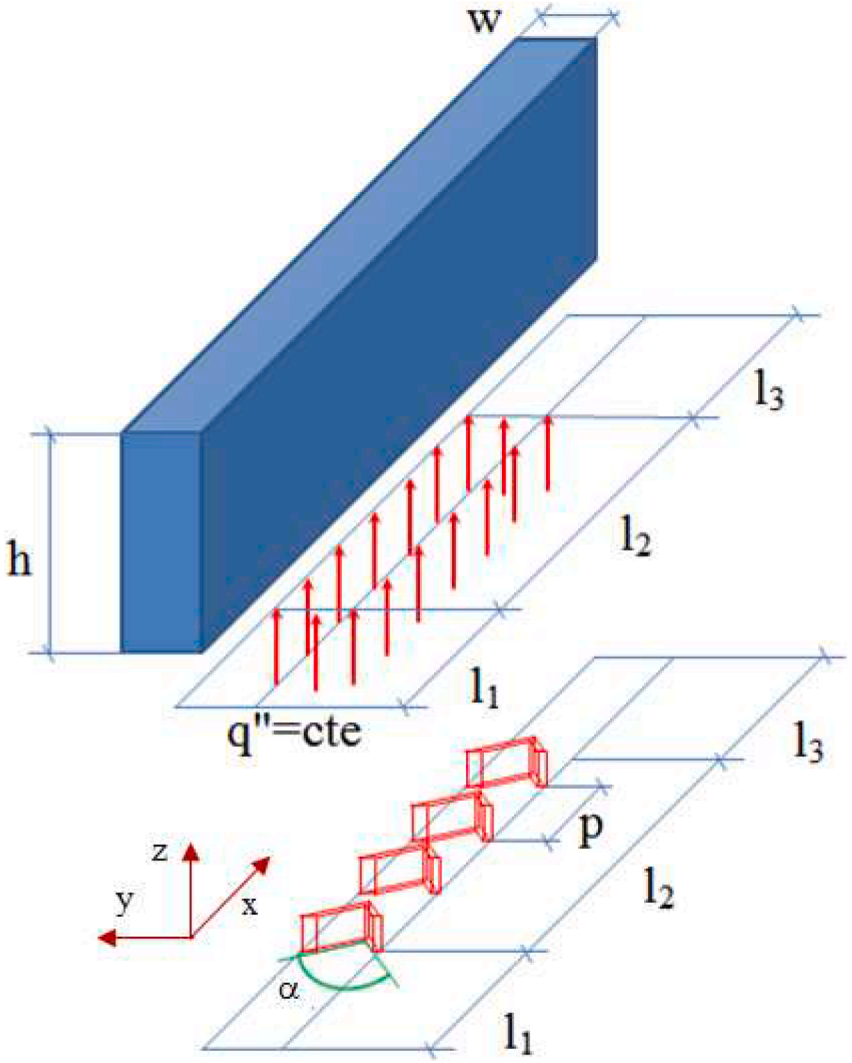

Fig. 1. Schematic and different variables of the system.

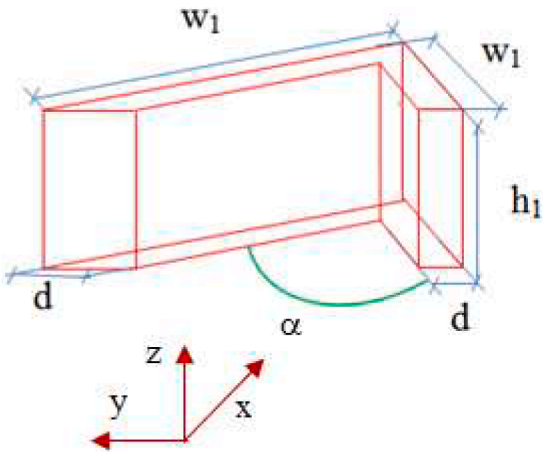

Fig. 2. Dimensions and variables of V-shaped ribs.

Table 1
Dimensions of the studied geometry (in micrometers).

l_3	l_2	l_1	α (deg)	L	h	w	d	w_1	h_1	p
2000	2000	3000	20-50	7000	100	60	10	Variable	25	400

two parallel plates with the presence of 4 square obstacles using FVM. Using the SIMPLER algorithm, they simulated the forced flow of NF for Re = 0.1-10 and φ = 0 to 0.04, taking into account the effects of sliding velocity and temperature jump. Their results showed that as the Knudsen number increases, the average Nusselt number (Nu_{ave}) and, therefore, S_{gen}, decrease. Moreover, as Re increases, Nu_{ave} and S_{gen} decrease. In addition, as φ increases, the temperature of NF decreases and as a result, the temperature gradient as well as heat transfer increases. Chtourou et al. [6] studied the heat transfer and laminar flow in a counter-flow plate heat exchanger with Y and C-shaped ribs to increase flow mixing. Using the computational fluid dynamics (CFD) method, they analyzed the geometric parameters' effect of obstacles inside the heat exchanger (such as geometry and pitch) on the flow characteristics, and thermal and hydrodynamic performance using the SIMPLE

Table 2
Thermophysical properties of solid nanoparticles and base fluid [15].

parameter	unit	Al_2O_3	Water
C_p	J/kg.K	765	4179
k	W/m.K	40	0.613
ρ	kg/m^3	3970	997.1
β	K^{-1}	8.5e-6	210×10^{-6}
μ	Pa.s	-	8.91×10^{-4}

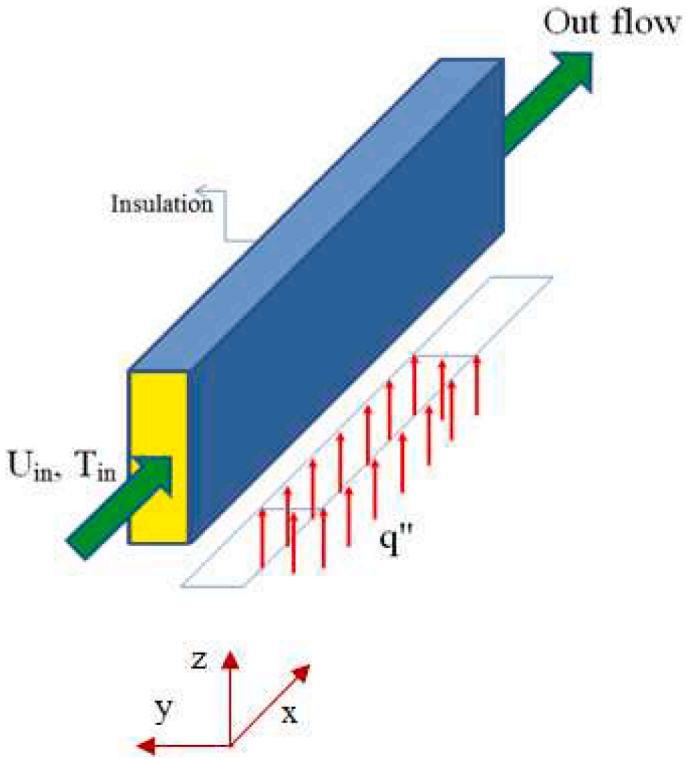

Fig. 3. Boundary conditions governing the present problem.

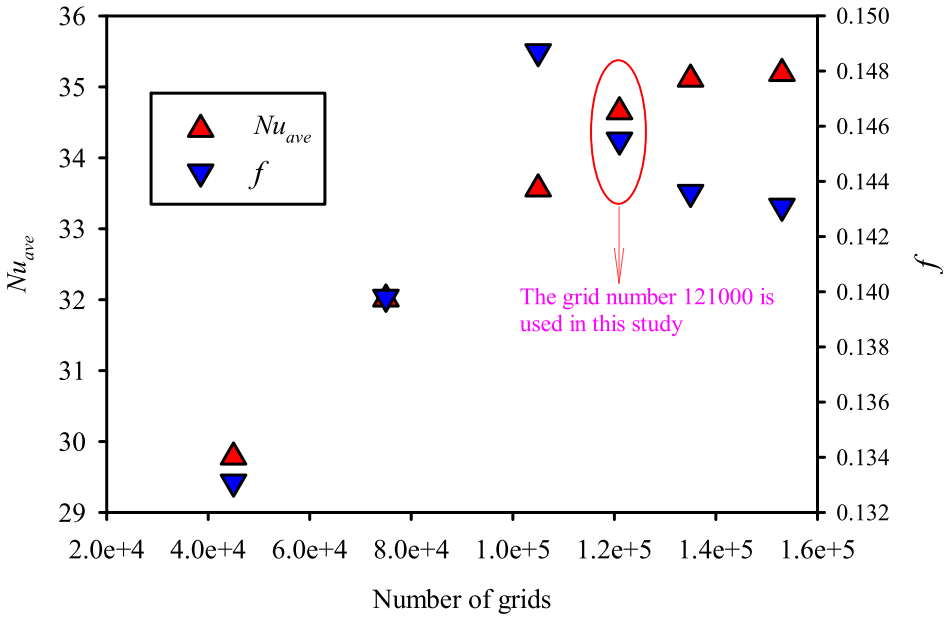

Fig. 4. Grid study in the present study.

Table 3
A study of the number of grids of the independence of the results.

Number of grids	Nu_{ave}	Error (%) $_{Nuave}$	f	Error (%) $_{f}$
45000	29.78	14.05	0.1331	8.52
75000	32.01	7.35	0.1398	3.92
105000	33.56	3.14	0.1487	2.1
121000	34.65	Basic mode	0.1455	Basic mode
135000	35.11	1.32	0.1436	1.3
153000	35.19	1.55	0.1431	1.65

algorithm in Re = 200-800. Their results show that the fins used increase the heat transfer and fluid mixing. Using Y and C-shaped fins increases the thermo-hydrodynamic efficiency by about %1.44 and %2.6 %, respectively. Al-Ali and Hamza [7] numerically investigated the effect of pitch changes of square obstacles in a rectangular channel with the presence of Water/TiO_2 nanofluid in φ = 0-0.04. In their investigation, they numerically studied the changes in the pitch of obstacles for the aspect ratio (AR) = 2.5, 3.125, 3.75, 4.375, and 5 for Re = 10-500 using FVM. The results showed that increasing the pitch of obstacles results in an increase in Nu. For this parameter, case I shows better results than case II because the constant distribution of the heat transfer rate in the whole Re range results in a thermal performance coefficient. In the case of constant heat flux (Case I) and for AR = 3.75, φ = 0.04, and Re = 500,

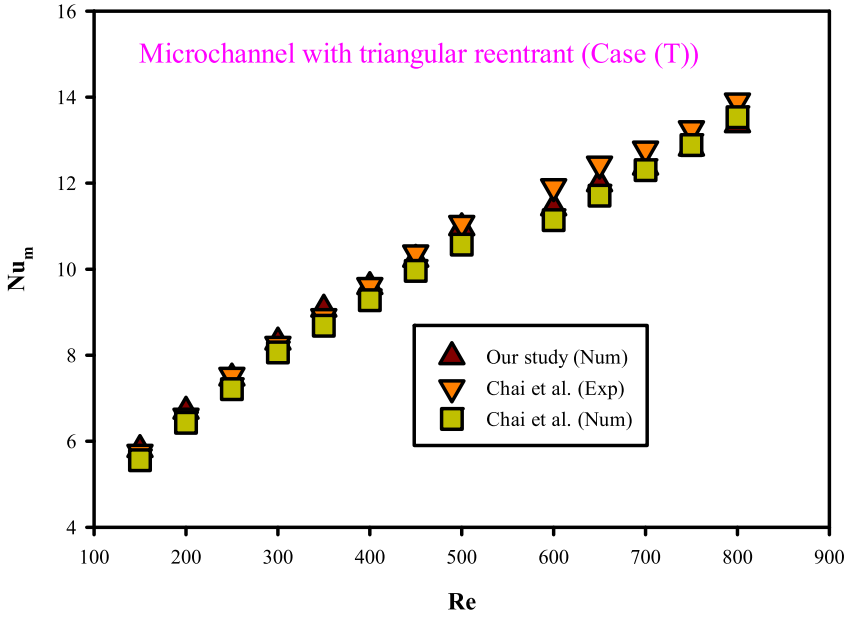

Fig. 5. Validation of the results with Chai et al. [28].

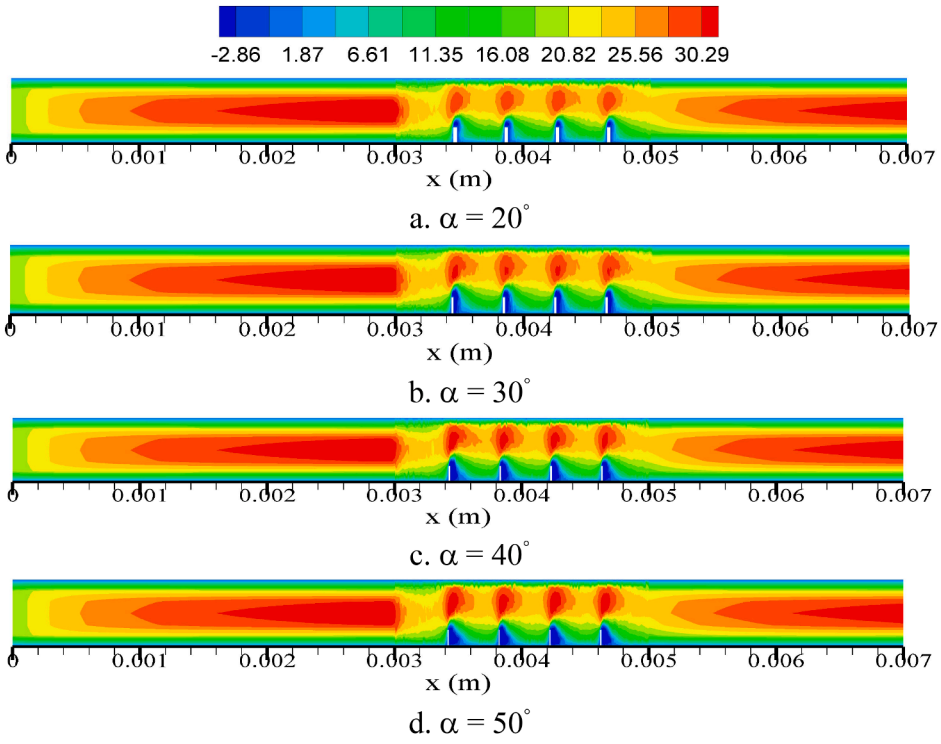

Fig. 6. Contours of changes in axial velocity (m/s) at different rib's attack angles (α).

the maximum average value of Nu is 10.76. Javaherdeh and Karimi [8] numerically studied the flow of NF in a rectangular channel for Re<1000 using FVM. Their results showed that the triangular, circular, and rectangular obstacles used with the presence of NF can affect the system and improve its thermal performance by 44 %. Among the investigated ribs, the rectangular ones can increase Nu by 30 % compared to the circular ribs. Hosseinirad et al. [9] numerically studied the presence of straight, curved, and wavy splitters on the hydraulic-thermal operation of the pin-fin plate heat exchanger using FVM with the SIMPLE algorithm. They analyzed the effect of the arrangement and shape of the gaps (square, rectangular) on the thermal behavior with Re = 50-250 in 3D analysis and confirmed their numerical simulations with an experimental study. Their results showed that replacing the design of indirect slots, i.e., curved and wavy, with straight dividers, reduces the heat exchanger's base temperature. The highest heat transfer coefficient occurs for the model equipped with and forward arrangement. The best overall hydrothermal performance is also observed for the model equipped with a bow and forward arrangement, and the increase in performance index is about 36 % more than the straight one. Rezaee et al. [10], using both experimental and numerical methods, analyzed the cooling of a pin-fin heat sink with pure water by changing the pin length and longitudinal pitch parallel with the flow direction. They demonstrated the characteristics of pressure drop and heat transfer of a finned heat sink with variable longitudinal pitch and pin length. The results showed that compared to the smooth heat sink, the reinforced models (along with pin-fin) have higher heat transfer coefficient and pressure drop. Increase values between 121.1 % and 73.3 % for heat transfer coefficient and between 284.6 % and 87.5 % for pressure drop were reported. Moreover, increasing the mass flow rate causes the hydrothermal performance of finned heat sinks to decrease. Salman et al. [11] gave a summary of several studies that focused on investigating heat transfer and fluid flow and types of microchannels, NFs, and microtubes (including behavior and properties). The purpose of this study is to express a clear view and a detailed summary of the effect of various parameters such as geometrical characteristics, boundary conditions, and fluid type. Behzadmehr and Mirmasoumi [12] evaluated the effects of the size of nanoparticles of NF on the heat transfer rate. In this research, the convective heat transfer of fully developed water-aluminum oxide NF is numerically studied. Also, the two-phase model has been used to investigate the flow parameters. The results of this article showed a significant increase in the convective heat transfer coefficient. Meanwhile, no significant change is observed in the hydrodynamic parameters. Akbari et al. [13,14] investigated the mixed convection heat transfer of a fully developed NF in inclined and horizontal tubes under a fixed heat flux. Their results show that φ has no important effects on the friction factor and hydraulic parameters. However, the angle of 45° leads to the maximum heat transfer coefficient.

Although many studies have been reported by researchers on the use of ribs and roughness in different geometries, the specific structure of the ribs in the microchannel and the presence of nanofluids using a two-phase mixture model distinguish the results of this study from other studies. V-shaped ribs with different attack angles are used to increase the heat transfer. Ribs are considered at the bottom of the rectangular microchannel. The nanofluid composed of water and different volume fractions of aluminum oxide is considered the working fluid. Using FVM, heat transfer and two-phase flow in a V-shaped ribbed microchannel are analyzed. The system is under a fixed heat flux. To model the two-phase flow, the two-phase mixture method is used. Moreover, the effects of the attack angle of V-shaped ribs and NF concentration are studied. The final results of heat transfer and hydrodynamic parameters in different attack angles are compared with each other.

2. Statement of the problem

In this research, the laminar mixed convection flow and heat transfer behavior of water-aluminum oxide NF inside a microchannel are numerically simulated in 3D space using FVM. To better estimate the behavior of the two-phase flow in the solid-liquid phase, the two-phase mixture model is used. To achieve higher heat transfer efficiency, V-shaped ribs with different attack angles are used at the bottom of the microchannel. Water-aluminum oxide NF is considered as the working

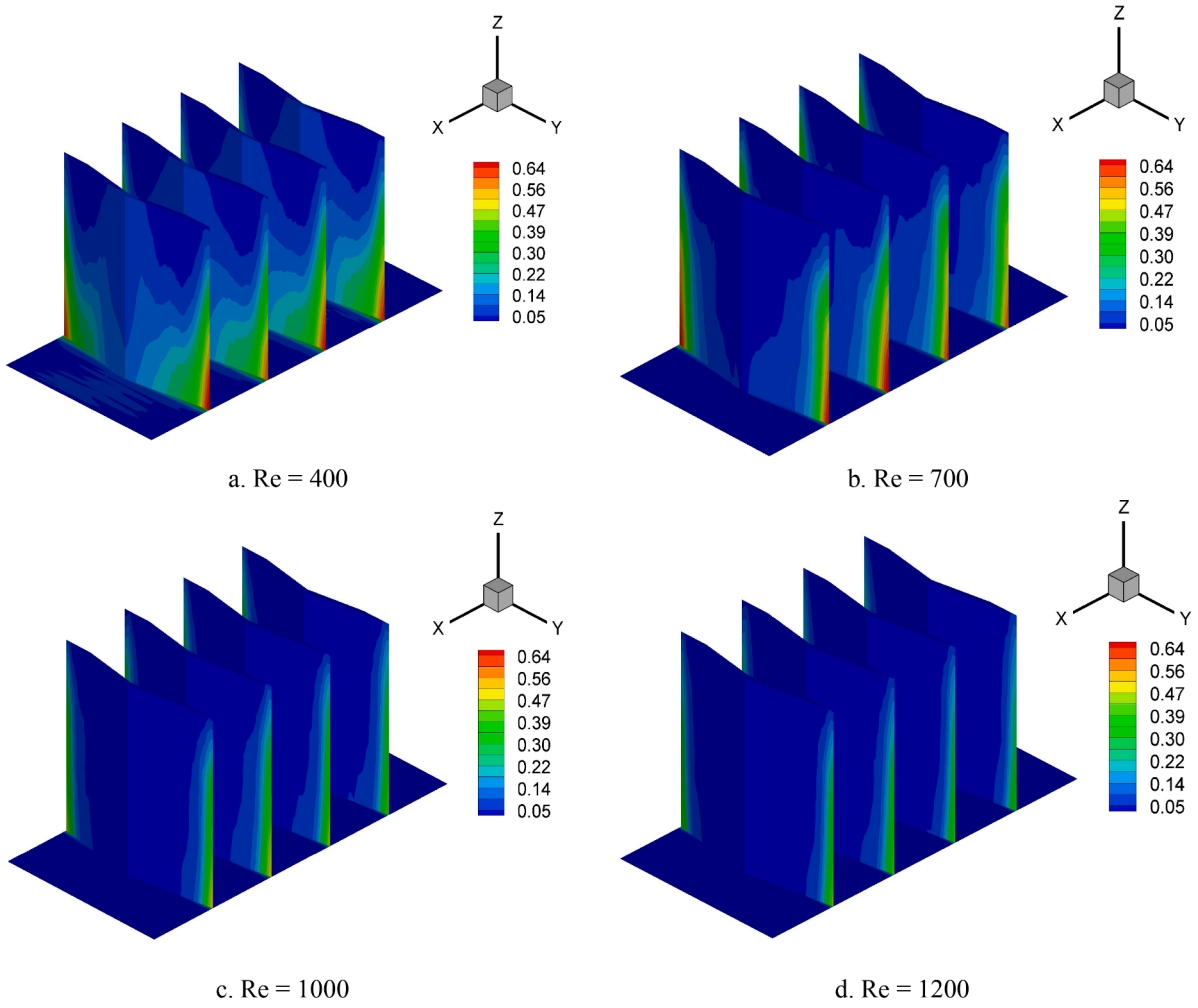

Fig. 7. Dimensionless temperature changes at $\alpha = 20^{\circ}$ and $\varphi = 0$ for Re = 400, 700, 1000 and 1200.

fluid with $\varphi = 0$, 0.02, 0.04 and Re = 400, 700, 1000, and 1200. Using FVM, two-phase heat transfer and flow of water-aluminum oxide NF in a microchannel equipped with V-shaped ribs are analyzed and investigated. A fixed heat flux equal to $q'' = 30000 W/m^2$ is exerted on the channel. The effects of nanoparticle concentration and the attack angle of the V-shaped ribs are also examined. The results obtained for different attack angles will be compared with each other. Fig. 1 describes the geometry and dimensions of the channel and Fig. 2 describes the variables and dimensions of the V-shaped ribs.

The above figures are related to the investigated geometry in this research. The problem includes a 3Drectangular microchannel, where L represents the microchannel length, h the channel height, w the channel width, d the rib length, w_1 the rib width, h_1 the rib height, p the rib pitch, and θ is the rib refraction angle. Table 1 illustrates all dimensions of different variables in the system.

In the corresponding geometry in Fig. 1, the parts of the channel are shown with l_1 and l_3 and other walls of the microchannel are insulated, and a fixed heat flux equal to $q'' = 30000\ W/m^2$ is exerted on the part shown with l_2 (the surface holding ribs). The number of ribs is 4 and they are empty (non-filled with material). Heat transfer and hydrodynamics of laminar flow of NF in a microchannel with $\alpha = 20^{\circ}$, 30°, 40°, and 50° are investigated. In this research, Gr = 1. Table 2 illustrates the properties of water-based fluid and nanoparticles.

The diameter of aluminum oxide nanoparticles is equal to 50 nm and the average water molecule diameter is 2 Angstrom [16]. Fig. 3 illustrates the boundary conditions considered in this study. According to Fig. 3, in the inlet section, the boundary conditions of the inlet fixed velocity and temperature are considered. In the outlet section, the condition of the outlet flow is used, and the boundary condition of the wall is used in the entire side walls throughout the channel. The side and top walls are insulated. The bottom wall of the microchannel is affected by the heat flux. No-slip and no-temperature jump boundary conditions are used in all walls.

The main goal of this study is to numerically simulate and investigate the fluid parameters and heat transfer of the two-phase flow of water-aluminum oxide NF in a microchannel equipped with V-shaped ribs. Among other objectives, the comparison of the parameters obtained from the numerical simulation for different rib' attack angles can be mentioned. Moreover, the behavior of two-phase flow in non-circular geometries is investigated. Considering the inlet length at the beginning of the microchannel, NF flow is hydrodynamically developed. The properties of NF are assumed to be dependent on φ and independent of temperature and Newtonian. Solid-liquid suspension in low concentrations is modeled as two-phase. A constant and uniform heat flux is applied to the bottom walls of the channel. The upper and side walls are insulated. Radiation effects are ignored. The "no-slip condition" is used on the walls.

3. Governing equations

3.1. Heat transfer and fluid flow equations

The two-phase mixture method is used in this study to simulate the two-phase flow of NF. In this regard, continuity, energy, and momentum

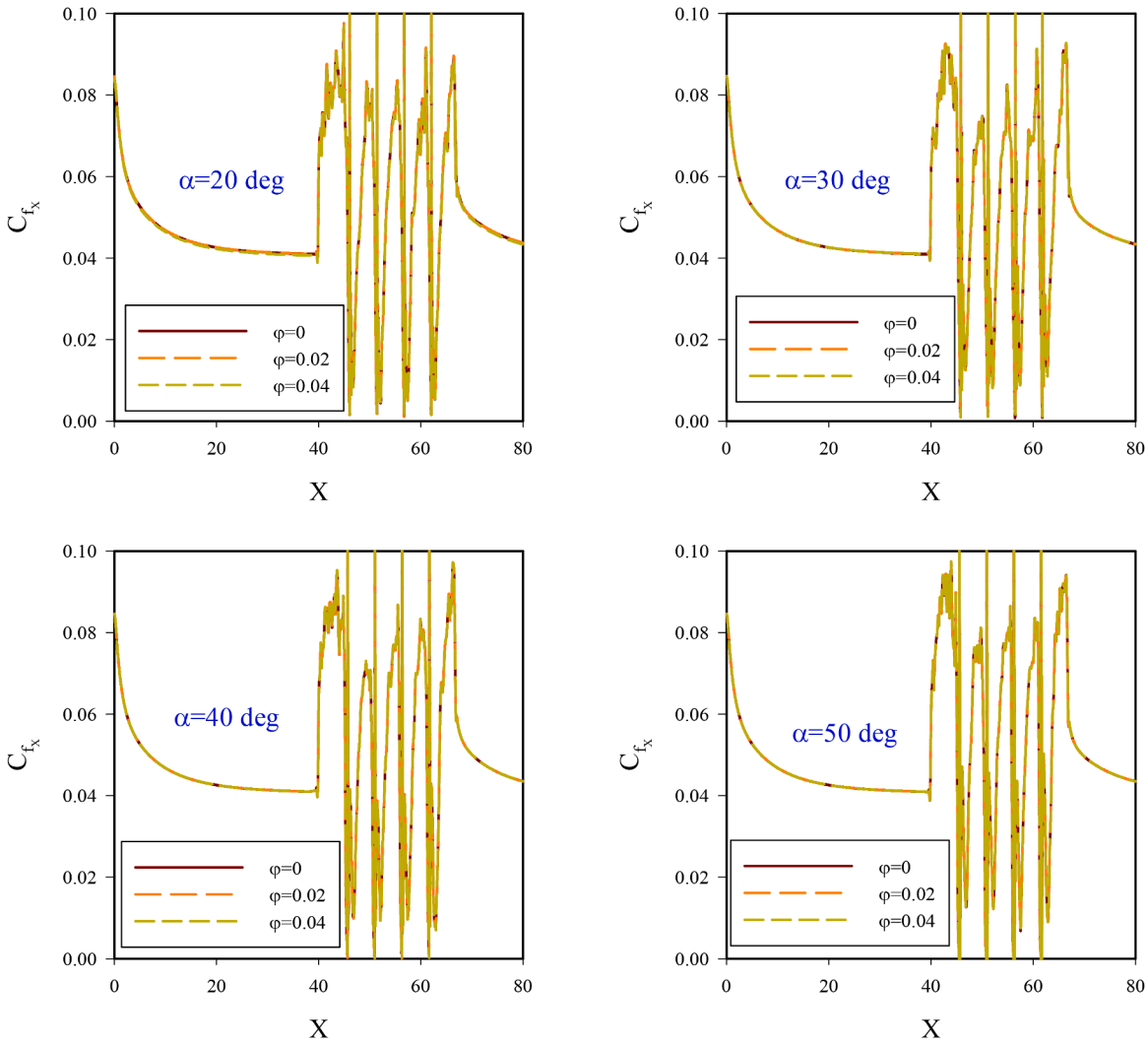

Fig. 8. Local friction factor at Re = 400 and different φ.

equations are used as follows [17,18].

Continuity equation,

$$\nabla.(\rho_m V_m) = 0 \tag{1}$$

Energy equation,

$$\nabla\left[\sum_{k=1}^{n}\varphi_k V_k(\rho_k H_k + P)\right] = \nabla.(k_m \nabla T) \tag{2}$$

Momentum equation,

$$\nabla.(\rho_m V_m V_m) = -\nabla P + \nabla[\mu_m \nabla V_m] + \nabla\left(\sum_{k=1}^{n}\varphi_k \rho_k V_{dr,k} V_{dr,k}\right) - \rho_{m,i}\beta_m g\,(T - T_i) \tag{3}$$

Volume fraction (φ) equation,

$$\nabla(\varphi_p \rho_p V_m) = -\nabla\left(\varphi_p \rho_p V_{dr,p}\right) \tag{4}$$

Where the amount of average mass speed (V_m) is calculated using the following equation,

$$V_m = \frac{\sum_{k=1}^{n}\varphi_k \rho_k V_k}{\rho_m} \tag{5}$$

In equation (3), $V_{dr,k}$, the drift velocity parameter for the secondary phase k, here refers to solid nanoparticles, is calculated as follows,

$$V_{dr,k} = V_k - V_m \tag{6}$$

Sliding speed (relative speed), which is the relative speed between base fluid particles and solid nanoparticles, is defined as follows,

$$V_{pf} = V_p - V_f \tag{7}$$

To define drag function and relative speed, the relations defined by Schiller and Naumann [19] and Manninen et al. [20] are used,

$$f_{drag} = \begin{cases} 1+0.15\mathrm{Re}_p^{0.687} & for \quad \mathrm{Re}_p \le 1000 \\ 0.0183\mathrm{Re}_p & for \quad \mathrm{Re}_p > 1000 \end{cases} \tag{8}$$

$$V_{pf} = \frac{\rho_P d_P^2 (\rho_P - \rho_m)}{18\,\mu_f f_{drag}}\, a \tag{9}$$

In the above equations, acceleration a is defined as follows,

$$a = g - (V_m \nabla) V_m \tag{10}$$

Where, $V_{dr,k}$ is the thrust velocity for the secondary phase z, V_m is the average (mass) velocity of the mixture and the indices P, T, φ, μ, and ρ are pressure, temperature, volume fraction, dynamic viscosity, and density, respectively. Moreover, the subscripts k, dr, and m express the secondary phase k, thrust, and mixture (solid-liquid phases), respectively.

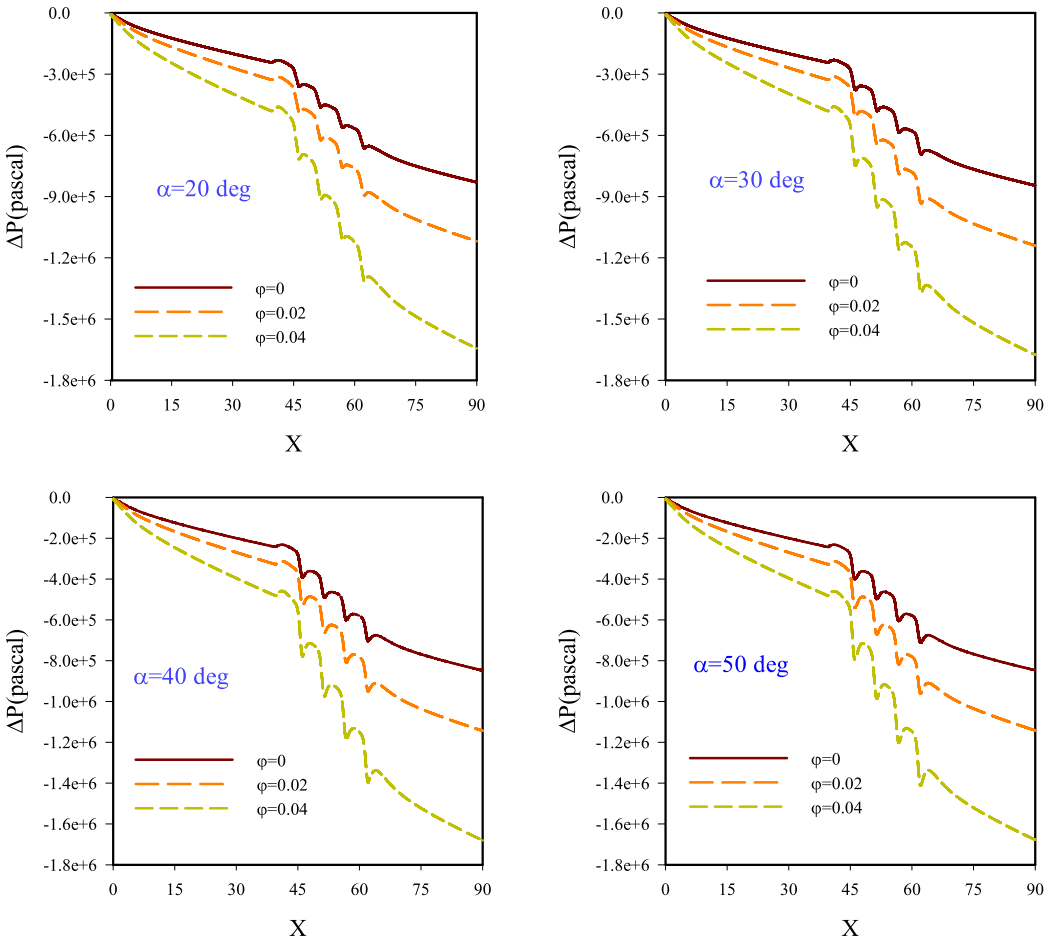

Fig. 9. Local pressure drop in the centerline of the microchannel for Re = 1000.

3.2. *Equations for calculating thermophysical properties of nanofluids*

Chon relation is used [21] to define the thermal conductivity of NF as follows,

$$\frac{k_m}{k_f} = 1 + 64.7\,\phi^{0.746}\left(\frac{d_f}{d_{np}}\right)^{0.369}\left(\frac{k_{np}}{k_f}\right)^{0.7476}\mathrm{Pr}^{0.9955}\,\mathrm{Re}^{1.2321} \tag{11}$$

Where all constants are defined as,

$$\mathrm{Re} = \frac{\rho_f k_b T}{3\pi\mu^2 l_f},\quad \mathrm{Pr} = \frac{\mu_f}{\rho_f \alpha_f},\quad \mu = A\times 10^{\frac{B}{T-C}},\ C = 140(K),$$
$$B = 247(K),\ A = 2.414\times 10^{-5}\,(Pa.s),\ T = T_{in} \tag{12}$$

The dynamic viscosity calculation relationship,

$$\mu_{\mathrm{eff}} = \left(123\phi^2 + 7.3\phi + 1\right)\mu_f \tag{13}$$

NF density [22],

$$\rho_m = \phi\rho_{np} + (1-\phi)\rho_f \tag{14}$$

Determination of specific heat capacity [22],

$$\left(\rho c_p\right)_m = (1-\phi)\left(\rho c_p\right)_f + \phi\left(\rho c_p\right)_{np} \tag{15}$$

The coefficient of thermal expansion is calculated from the following equation [23],

$$\frac{\beta_{eff}}{\beta_f} = \left[\frac{1}{1+\frac{(1-\varphi)\rho_f}{\varphi\,\rho_P}}\times\frac{\beta_P}{\beta_f} + \frac{1}{1+\frac{\varphi\,\rho_P}{(1-\varphi)\rho_f}}\right] \tag{16}$$

The following definitions are used to dimensionless the software output parameters,

$$Y = \frac{y}{H}$$
$$Z = \frac{z}{H}$$
$$\mathrm{Pr} = \frac{\upsilon_f}{\alpha_f}$$
$$X = \frac{x}{H} \tag{17}$$
$$\theta = \frac{T - T_c}{\Delta T}$$
$$\Delta T = \frac{q''_0 H}{k_f}$$

The friction factor is one of the parameters that is used to check the microchannel performance [24],

$$C_f = \frac{2\times\tau_w}{\rho u_{in}{}^2} \tag{18}$$

The average Nu is also another factor in heat transfer that expresses the convection heat transferred to the conduction heat transferred, and it is obtained from the following equation [25],

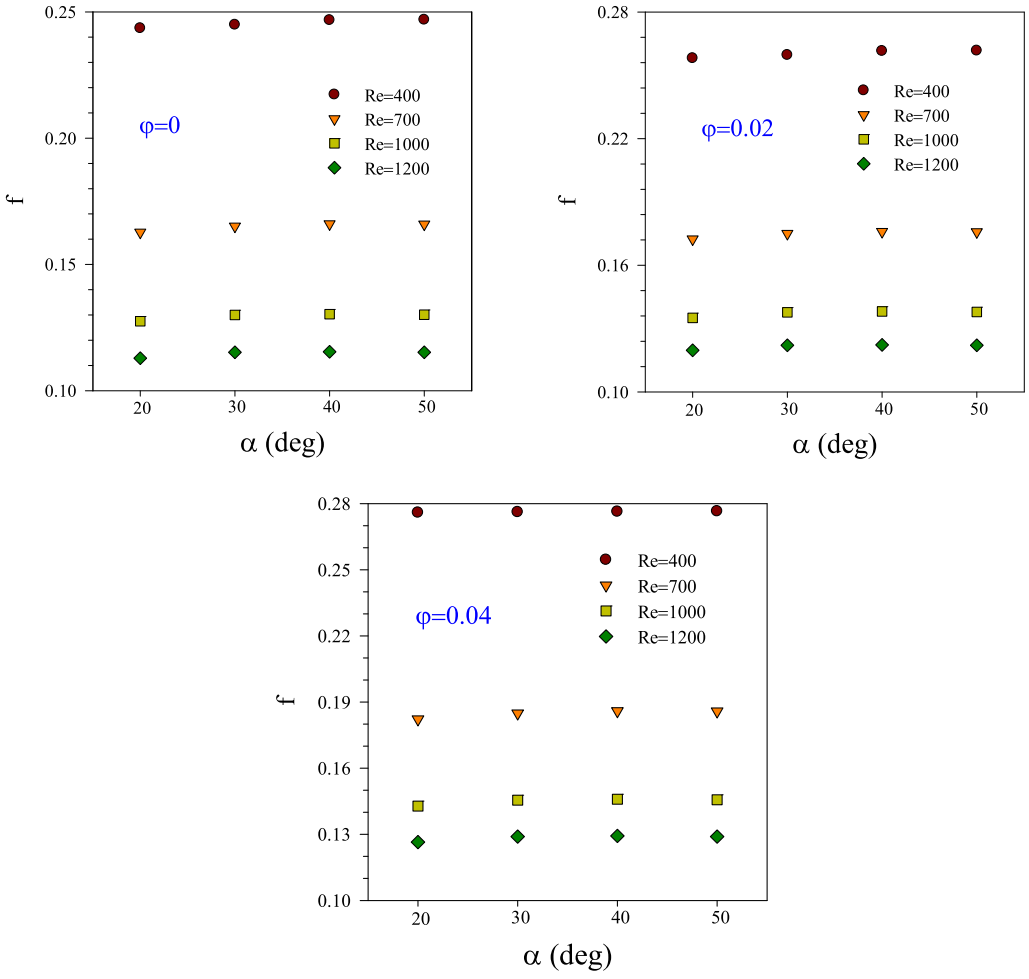

Fig. 10. Variations of average friction factor at different attack angles.

$$Nu_x = \frac{h \times H}{k_f} \rightarrow Nu_{ave} = \frac{1}{L}\int_0^L Nu_x(X)\,dX \tag{19}$$

NF flow in microchannel includes pressure drop (ΔP) which is calculated by,

$$\Delta P = P_{in} - P_{out} \tag{20}$$

The following equation is used to calculate Moody's friction factor f,

$$f = \frac{2 \times \Delta P \times D_h}{\rho \times L \times u_{in}^2} \tag{21}$$

The thermal-fluid performance, which is defined as PEC, is defined as [26],

$$PEC = \frac{\left(\frac{Nu_{ave}}{Nu_{ave,\varphi=0}}\right)}{\left(\frac{C_f}{C_{f,\varphi=0}}\right)^{(1/3)}} \tag{22}$$

Gr and Re for NF flow inside the nanochannel are calculated as.

$$Gr_{D_h} = \frac{g \times \beta_{eff} \times {D_h}^4 \times q''}{k_{eff} \times {\nu_{eff}}^2} \tag{23}$$

$$\mathrm{Re} = \frac{\rho_{eff} \times D_h \times V_m}{\mu_{eff}} \tag{24}$$

The amount of increase in entropy due to the heat transfer and flow friction, which is defined as total entropy ($S_{gen,tot}$), is calculated as [27],

$$S_{gen} = \frac{k_{eff}}{\overline{T}^2}\left[\left(\frac{\partial \overline{T}}{\partial x}\right)^2 + \left(\frac{\partial \overline{T}}{\partial y}\right)^2 + \left(\frac{\partial \overline{T}}{\partial z}\right)^2\right] + \frac{\mu_{eff}}{\overline{T}}\left\{2\left[\left(\frac{\partial \overline{u}}{\partial x}\right)^2 + \left(\frac{\partial \overline{v}}{\partial y}\right)^2 + \left(\frac{\partial \overline{w}}{\partial z}\right)^2\right] + \left(\frac{\partial \overline{u}}{\partial x} + \frac{\partial \overline{v}}{\partial y} + \frac{\partial \overline{w}}{\partial z}\right)^2\right\} \tag{25}$$

4. Solution method and assumptions, grid study and validation

4.1. Solution Method and Assumptions

The forced and constant flow of NF is modeled in this study. NF properties are Newtonian, independent of temperature, and constant (homogeneous). The two-phase mixture method is used for numerical solutions and NF flow is modeled as two-phase flow. This research was solved using a finite volume method and a computer code in three-dimensional space. SIMPLE algorithm and second-order discretization are used to solve the equations. Moreover, the radiation effects are neglected. The nanofluid flow is assumed to be incompressible and laminar. For velocity on the walls, the no-slip boundary condition is used. The amount of 10^{-6} is used as the maximum numerical solution residual.

4.2. Mesh study

To numerically simulate the solution field using FVM, an

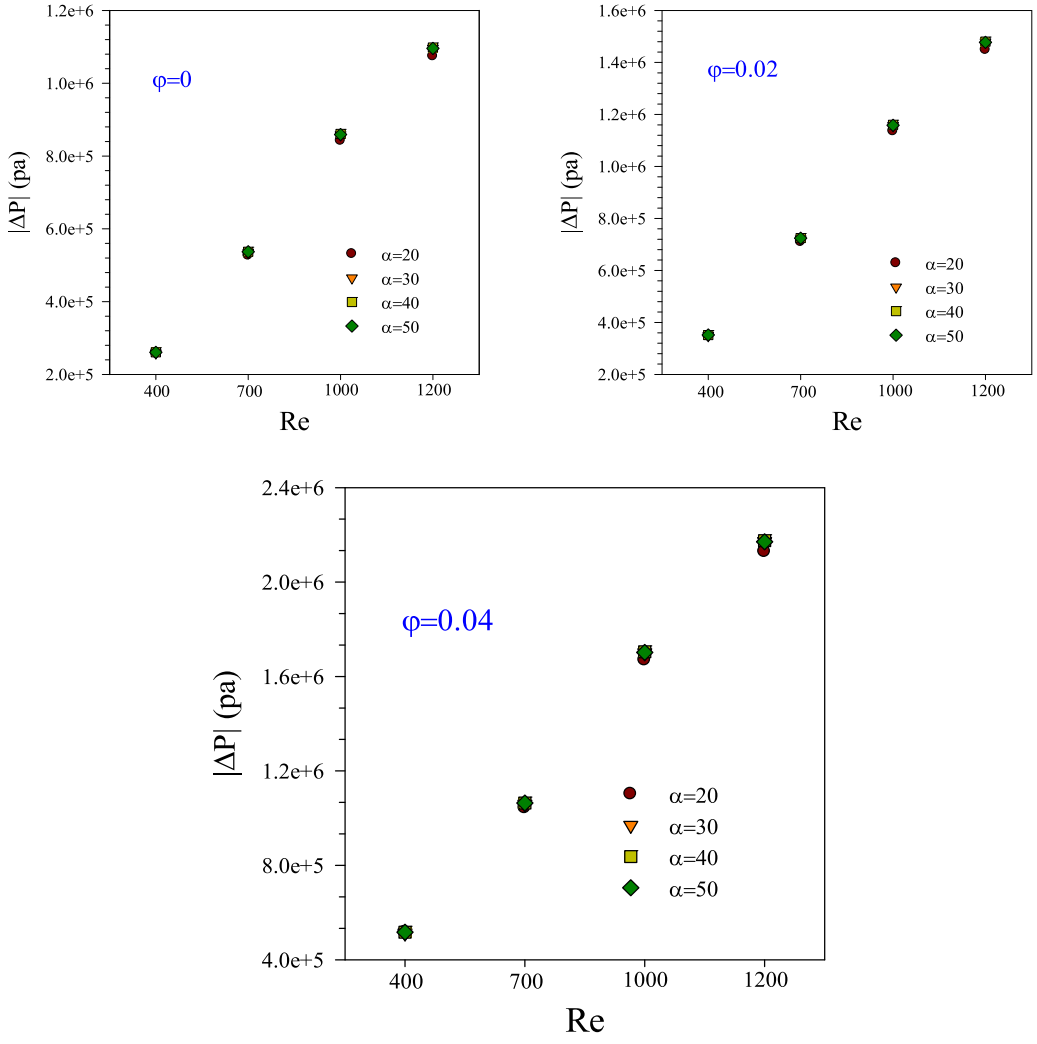

Fig. 11. Average pressure drop at different α and different Re.

unorganized grid is used. The number of grids was selected from (45000) to (153000) according to Fig. 4. To be sure of the independence of the results from the grid number, the parameters of Nu_{ave} on the lower wall of the microchannel and f at the attack angle of $\alpha = 30^{\circ}$, at Re = 1000 and $\varphi = 0.04$ are changed. According to the changes of parameters of Nu_{ave} and f, the amount of error was obtained according to Table 3. Accordingly, the grid number of 121000 is the most optimal and suitable state. This is because both Nu_{ave} and f changes have the least error and the resulting answers are grid number independent. Therefore, the grid number 121000 is used.

4.3. Validation

To validate, the experimental-numerical results of Chai et al. [28] are used to be compared with the results of the present study. Chai et al. [28] investigated numerically and experimentally the convection heat transfer (forced) of the laminar flow of water in a smooth rectangular 3D microchannel experiencing a sudden contraction-expansion using holes with circular and triangular shapes for Re<1000. In their modeling, to use proposed microchannels to remove and expand the thermal boundary layer, they investigated the heat transfer and flow parameters. According to Fig. 5, the changes in Nu_{ave} for the T structure micro-channel in the range of Re = 150 to 900 are compared with numerical and experimental results. By comparing the obtained results, it can be seen that the assumptions considered for the numerical solution in this research have a suitable accuracy and, therefore, the results have a good accuracy.

5. Results and discussion

Many studies have been conducted by researchers to investigate flow distribution and heat transfer numerically [29–33]. In this study, the results include friction factor (f), Nusselt number (Nu), pressure drop (Δp), dimensionless temperature (θ), thermal-fluidic efficiency factor (PEC), velocity and temperature contours, and S_{gen}. All calculations are done for Re = 400, 700, 1000, and 1200 and for φ = 0-0.04. Moreover, the attack angle of V-shaped ribs varies from 20° to 50°.

5.1. Velocity contours

Axial velocity contours are presented in Fig. 6. These include all results at different α, at Re = 1200 and φ = 0.04 in the Y = 0.4 plane. The amount of changes in α can have a great effect on the gradients of the speed of flow passing over the rib. According to the contours, the maximum fluid velocity is seen in the areas above the ribs. This behavior is caused by the narrowing of the side section of the channel. After the fluid passes over the ribs, with the increase of α, the velocity gradients undergo significant changes. This behavior is shown in the contours. A

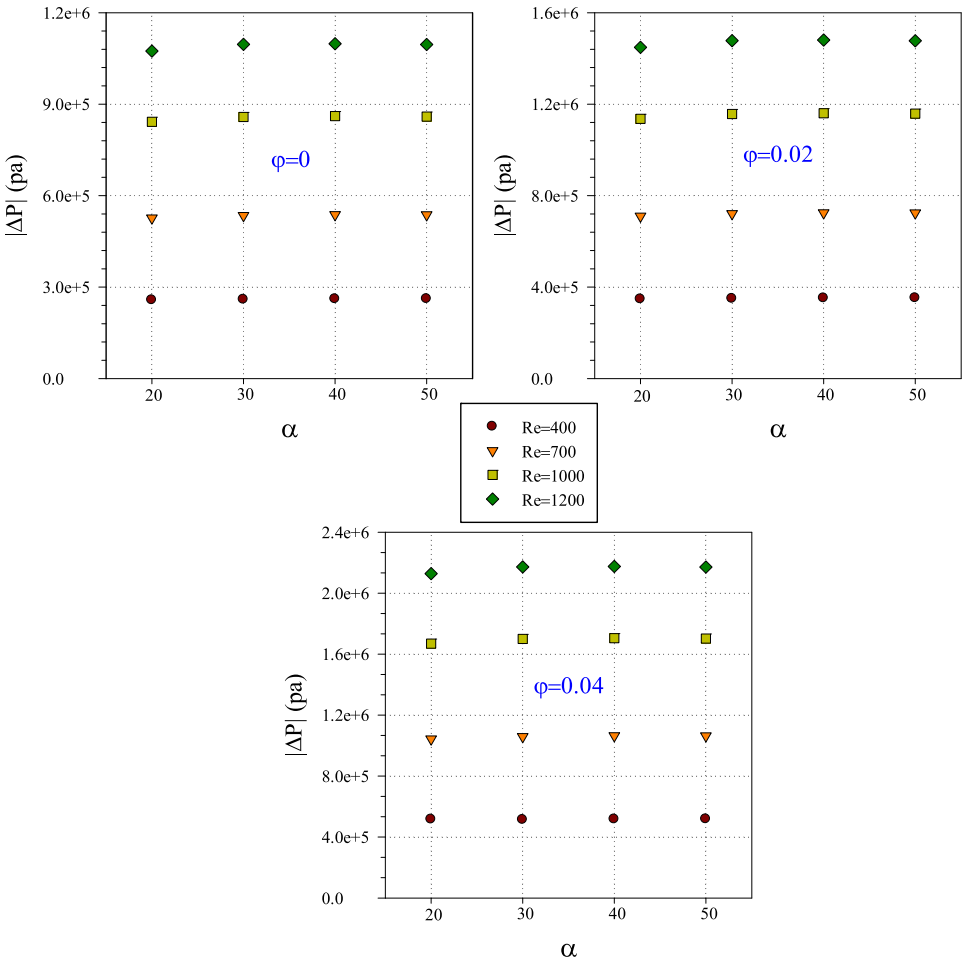

Fig. 12. Average pressure drop at different attack angles.

reverse velocity gradient of the fluid is seen in the areas after the ribs. With the increase of α, the wake area increases with reverse gradients. For all different attack angles, the behavior of axial velocity contours is the same.

5.2. Non-dimensional temperature contours

Dimensionless temperature (θ) contours at $\alpha = 20^\circ$ and $\varphi = 0$ for Re = 400, 700, 1000, and 1200 are presented in Fig. 7. The dimensionless temperature contours for the same level are compared with each other. In general, increasing the fluid velocity increases the fluid momentum. This behavior covers all the warm surfaces of the ribs (back and front areas of the ribs). At lower Re, parts with lower heat transfer (i.e., hot areas) can be seen in the areas behind the ribs. These areas are shown in red in the contours. The creation of hot areas on rib surfaces occurs mostly in the parts where the fluid momentum decreases. Usually, these areas are at the junction of the edge of the ribs with the side walls of the microchannel and the areas connected to the bottom of the microchannel. The highest amount of hot areas behind the ribs is at Re = 400 and the lowest at Re = 1200.

5.3. Friction factor and pressure drop

Fig. 8 shows the variations of local friction factor (C_{fx}) at $\alpha = 20^\circ$ to 50°, Re = 400, and $\varphi = 0$ to 0.04. According to Fig. 8, the changes in C_{fx} depend on the changes in the velocity gradients in the areas close to the surfaces. The maximum amount of changes in C_{fx} is in the areas of fluid movement in the ribbed parts and after that. According to the diagrams, the behavior of C_{fx} is the most effective for the first to third ribs. Sudden jumps in the graphs are caused by the collision of the fluid with the ribs and the fluid's direction change at the edge of the ribs. In addition, the maximum amount of sudden jump can be seen at $\alpha = 40^\circ$ and 50°, and this amount decreases gradually with the decrease of α. For almost all the graphs, there are no specific changes in C_{fx} variations in the last rib.

In the range of examined Re in this research, because the fluid velocity is high enough and the fluid does not have enough time to contact all the rib's surfaces, the level of the friction factor graphs is about 0.1. Moreover, increasing the fluid speed results in decreasing C_{fx}. Therefore, increasing φ does not show significant changes in C_{fx}. But in general, increasing φ can increase the friction factor. Fig. 9 shows ΔP changes in the center line of the microchannel for Re = 1000 and in $\varphi = 0$, 0.02 and 0.04. These diagrams have been drawn to determine the behavior of ΔP in the center line of the flow for different α and φ. In ΔP diagrams, because the fluid changes the velocity components by moving along the ribbed path, the fluid momentum decreases and the pressure drop increases. This amount is significant in the areas behind the ribs. In all graphs, local pressure drop changes in the areas before and after the ribs have the same trend to some extent. In the ribbed area, the fluctuating changes in pressure drop are caused by moving along the ribbed path. In all graphs, increasing φ can increase fluid viscosity and density. This behavior increases fluid momentum depreciation and causes a pressure drop. Also, increasing α causes the creation of stronger vortices and higher fluid momentum depletion. With the increase of α, the eddies and velocity gradients separated from the rib's surfaces penetrate the center

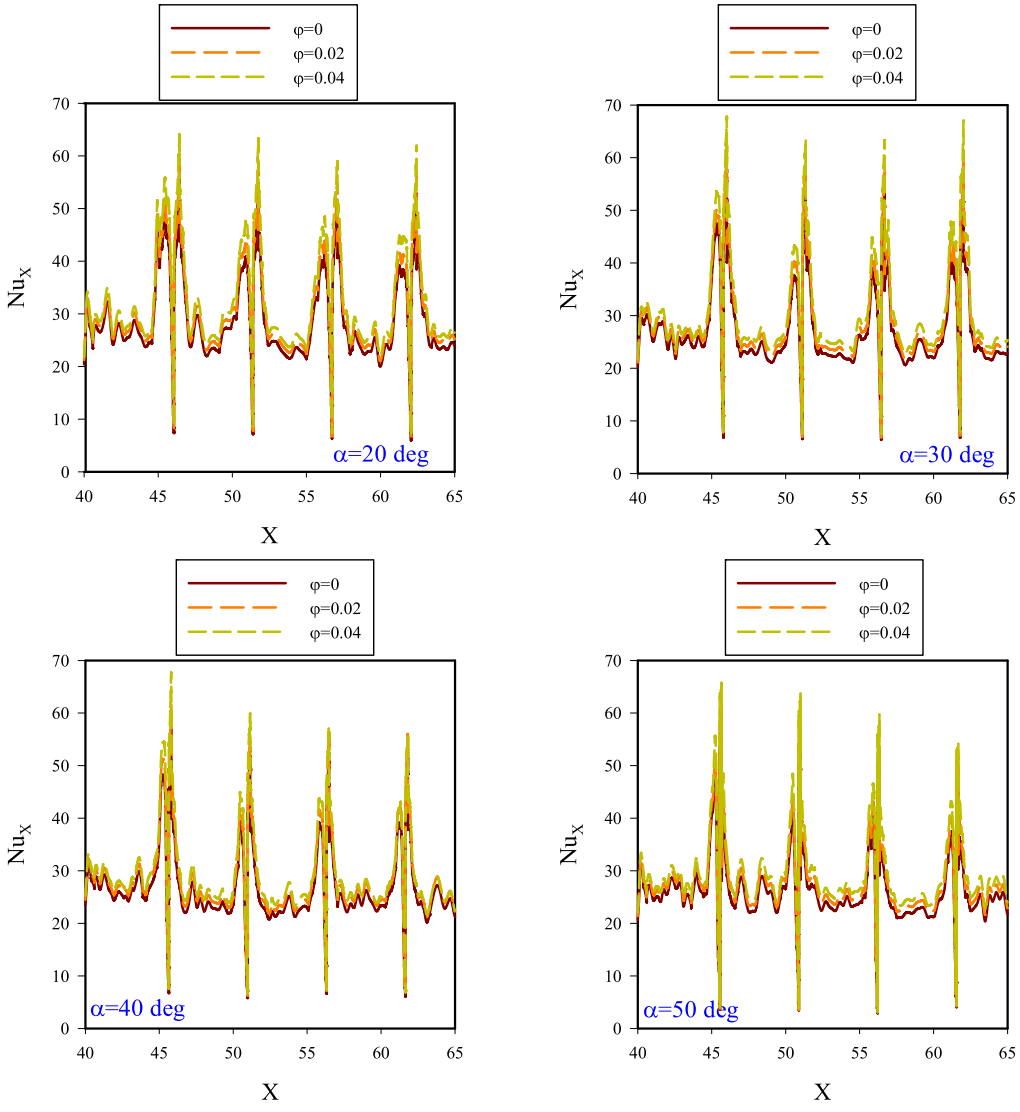

Fig. 13. Nu_{ave} along the length of the ribbed area at Re = 1200.

of the flow. Therefore, the behavior of the local pressure drop in the serrated areas is affected. Among all cases, the maximum ΔP corresponds to α = 50° and the lowest one corresponds to α = 20°.

Fig. 10 compares the graphs of the average friction factor (f) at different α, φ, and Re. According to the graphs, increasing the fluid speed leads to a decrease in f. In all diagrams, the highest value of f corresponds to the lowest fluid speed (Re = 400). An increase in φ can also increase f. This behavior is caused by an increase in pressure drop. In examining the factors that affect the hydrodynamic behavior of the flow in and therefore the behavior of f, α is important. It is seen in all the graphs that the increase in α causes an increase in f. This is because of the existence of stronger vortices and higher momentum depreciation at higher α. At α = 20°, the friction coefficient is minimal because the fluid in its movement path feels the existence of the ribs less. At α = 50°, because the fluid in contact with the ribs has a high-velocity drop and the creation of stronger vortices, the friction coefficient is maximum.

Overall, with increasing the volume fraction of solid nanoparticles relative to the base fluid, the friction coefficient increases by 9 to 15 percent. With increasing the angle of attack, the friction coefficient decreases by less than 5 percent. Increasing the Reynolds number from 400 to 1200 can also reduce the friction coefficient by 1.1 to 1.23.

The average pressure drop at different α and different Re is presented in Fig. 11. These diagrams are drawn to evaluate the effect of changes in α on the ΔP_{ave} behavior. By increasing the fluid speed, the growth of the vortices resulting from the collision of the fluid with the ribbed surfaces increases.

At low Re, these vortices will not have much effect on the pressure drop. The presence of a rib with a higher α can also strengthen vortices. The increase of φ can also affect the behavior of the average pressure drop. In all diagrams, by increasing Re, φ, and α, the pressure drop increases significantly. But at low Re, due to the mentioned reasons, the amount of pressure drop does not have a special dependence on the increase of α and the increase of φ. Fig. 12 illustrates the changes in average pressure drop in different α, Re, and φ.

According to the diagrams in Fig. 12, at Re = 700 and 1000, the increase in pressure drop and its dependence on α become important. At Re = 400 and 700, pressure drop changes do not have a special dependence on the rib's form. In all diagrams, increasing φ causes an increase in the viscosity and adhesion of the fluid to the surfaces of the microchannel, especially the ribbed areas. This behavior strengthens and sustains the creation of velocity gradients and significantly increases the pressure drop.

5.4. Nusselt number

Fig. 13 illustrates the changes of the local Nusselt number (Nu_x)

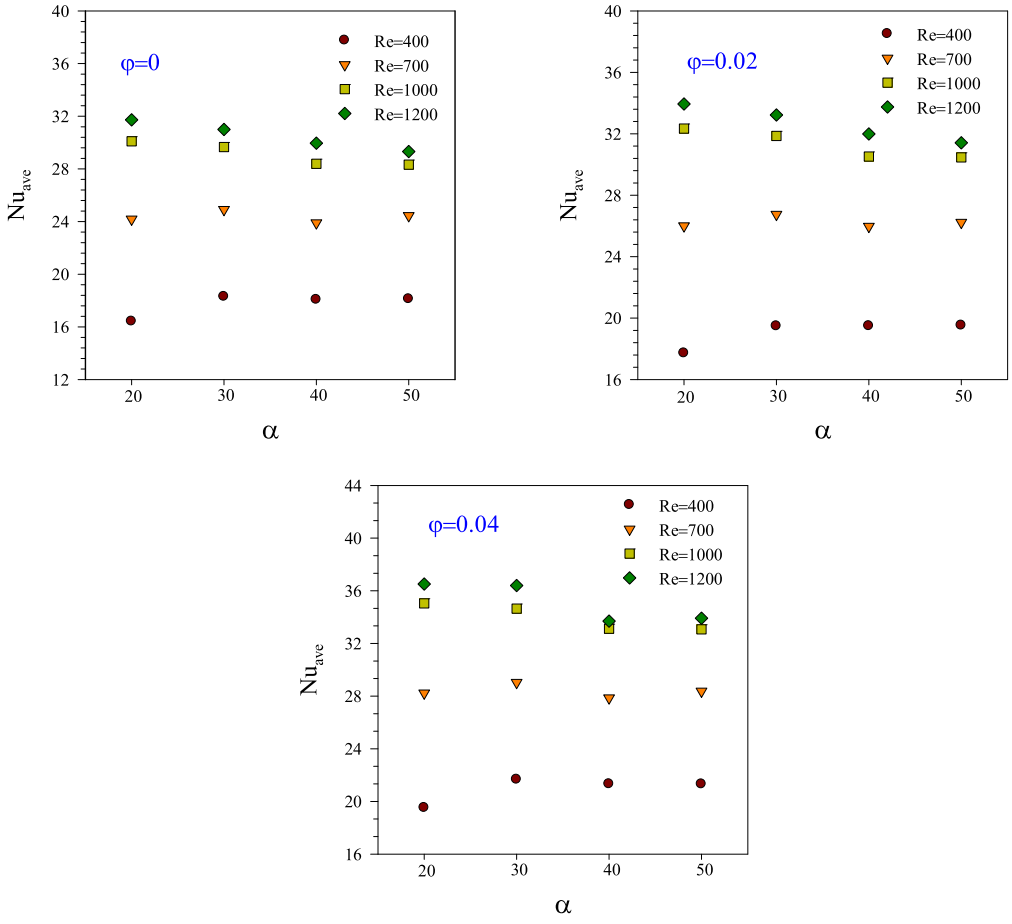

Fig. 14. Variations of average Nusselt number (Nu_{ave}) at different α.

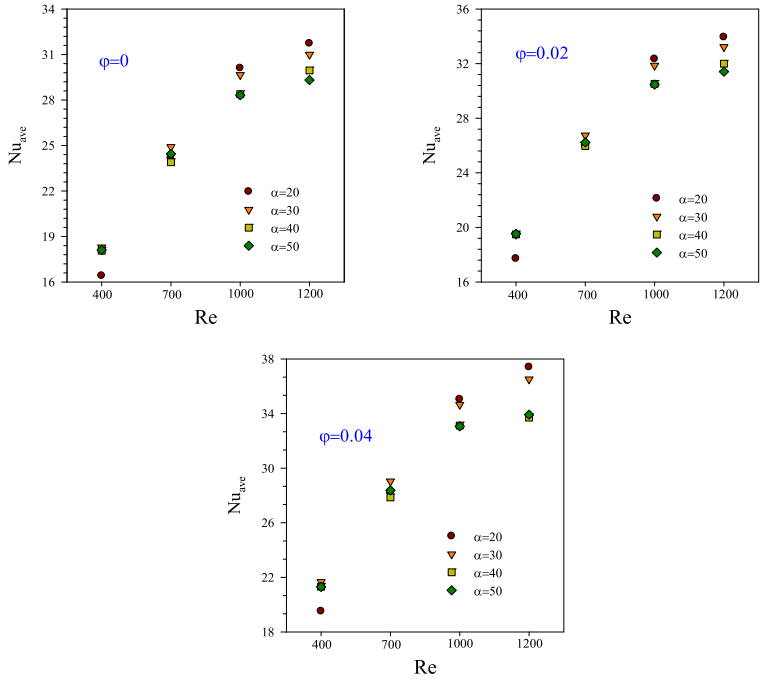

Fig. 15. Nu_{ave} at different Re, φ, and α.

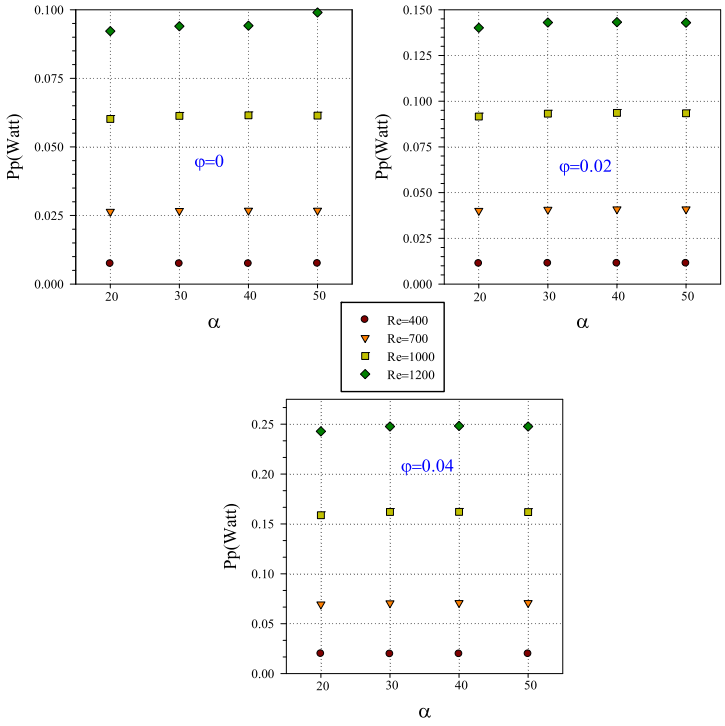

Fig. 16. Pumping power (P_p) in different φ.

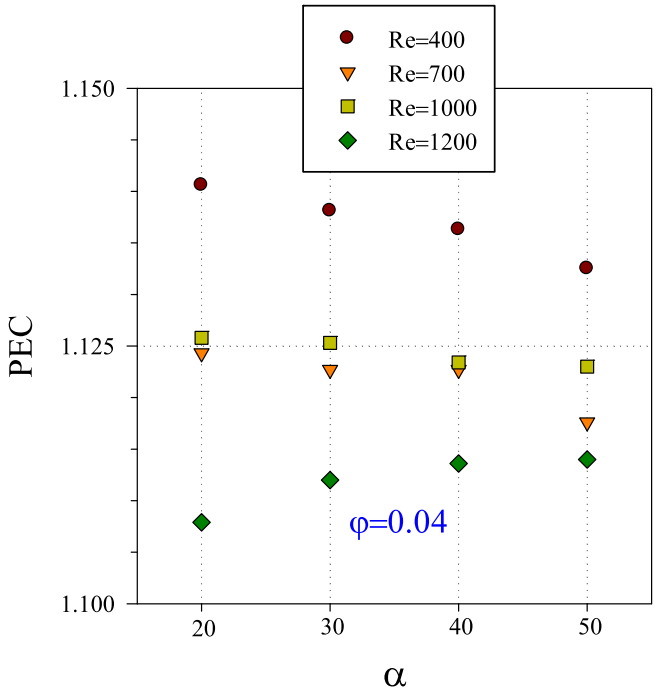

Fig. 17. Variations of thermal-fluidic efficiency parameter at different α.

along the length of the ribbed area at Re = 1200 for different α. With the movement of the fluid along the ribbed surfaces, due to the presence of obstacles and roughness, the three-dimensionality of the flow, the creation of transverse velocity gradients due to the existence of V-shaped ribs and the deviation of the flow in transverse directions, the fluid velocity undergoes certain changes. Therefore, the above factors cause a change in the behavior of the heat transfer coefficient, fluid displacement, and heat transfer and affect Nu_x. In the ribbed areas of the microchannel, the increase in φ and the flow pattern will have a big effect on the increase of Nu and changes in heat transfer. According to the presented results, the mentioned factors were also involved in changing the behavior of pressure drop parameters and friction factors. In all investigated cases, the increase in φ due to the thermal conductivity increase, Nu increases significantly. Moreover, increasing α

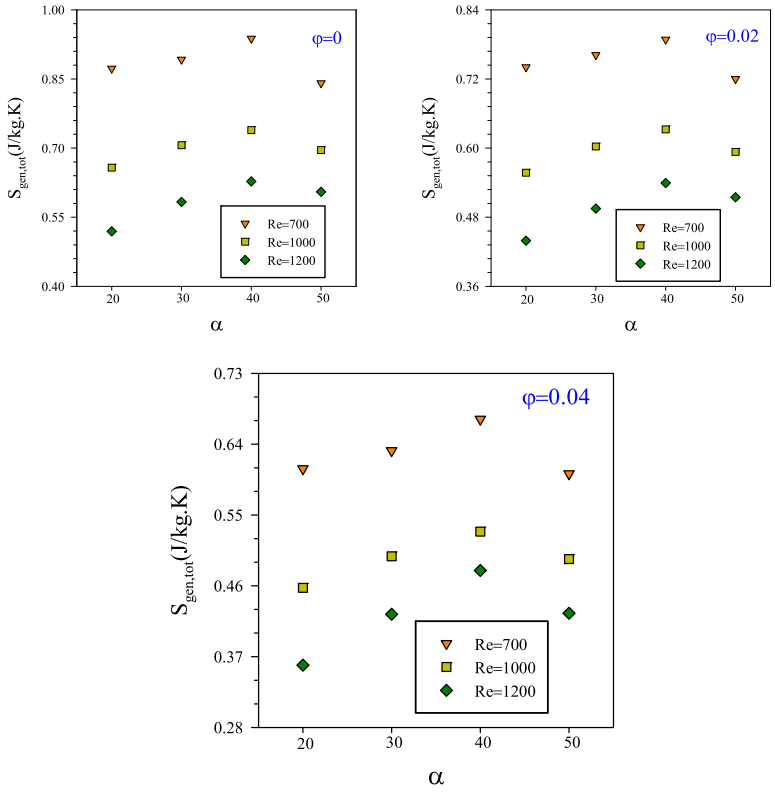

Fig. 18. Total entropy generation $S_{gen,tot}$ at different α, φ, and Re.

creates stronger longitudinal vortices that cause flow mixing. Changes in the behavior of Nu_x in the ribbed region of the microchannel for α = 40° and 50° have similar behavior. On the other hand, the decrease of α strengthens the transverse flow vortices.

Fig. 14 compares the changes of Nu_{ave} at α = 10° to 50°, Re = 400, 700, 1000, and 1200 and φ = 0, 0.02, and 0.04. These graphs compare Nu_{ave} in different Re in each φ. According to the graphs of Nu_{ave}, it can be seen that the presence of ribs with higher α causes stronger longitudinal vortices, and the presence of ribs with lower α causes transverse vortices in the fluid flow.

At Re = 400, longitudinal vortices increase heat transfer and cause better mixing of the flow. In addition, the strengthening and growth of transverse vortices are not significant. Therefore, increasing α leads to increasing Nu. At Re = 700, the presence of longitudinal and transverse vortices causes different behaviors in different α. In Re = 1000 and 1200, increasing the heat transfer is possible by choosing a rib with a lower α. At Re = 1000 and 1200, due to the accumulation of fluid motion, longitudinal vortices in the studied geometry do not create higher mixing. Instead, the presence of transverse vortices causes better fluid mixing and better heat transfer. In all investigated cases, a significant increase in heat transfer is seen by increasing φ [32–38]. This behavior is caused by the increase in thermal conductivity and the change in the thermophysical properties of the base fluid at higher φ. According to the behavior of the average Nusselt number, with increasing volume fraction of solid nanoparticles compared to the base fluid, the Nusselt number increases by 5 to 17 %. With increasing the angle of attack, the average Nusselt number also decreases by less than 14-16 %. Increasing the Reynolds number from 400 to 1200 can also increase the average Nusselt number by 1.15 to 1.35 times. Fig. 15 compares the values of Nu_{ave} in different Re, different φ, and different α. This investigation was carried out to quantitatively determine Nu_{ave} with the changes of α in each φ. As the diagrams show, the highest amount of Nu_{ave} occurs in Re = 700 to 1200 at α = 20°. The behavior of Nu_{ave} at Re = 400 is such that the highest amount corresponds to α = 30°, 40°, and 50°. At α = 20°, the lowest value of Nu_{ave} is also gained. It is recommended that in industrial applications of heat transfer, improving devices similar to the design used in the present study, to achieve the maximum increase in heat transfer, V-shaped ribs with α = 20° should be used at Re>700. In Re<400, ribs with an α higher than 20° should be used.

5.5. *Pumping power*

Fig. 16 examines the required pumping power (P_p) at φ = 0 to 0.04, for different Re and different α. With the movement of the fluid between the roughnesses (or ribs) and also the interlayer movement in different layers of the fluid, as well as the movement of the fluid on the solid surfaces and walls of the microchannel, the kinetic energy of the cooling fluid decreases. In the examined graphs, it can be seen that increasing the fluid speed requires increasing the pumping power [39–43].

Increasing the density and viscosity of the fluid as a result of the velocity boundary layer effect increase, the fluid becoming heavier and the level of layer resistance against the fluid movement and the increase in shear stress on the surfaces and walls of the microchannel, the fluid momentum has decreased significantly and, therefore, the amount of pumping power increases. Hence, at higher φ, the pumping power plots have an increasingly flat surface. It can be seen in the examined α range that at a Re = 400, the increase in α does not have a particular effect on the increase in pumping power. At Re>400, the increase of α increases the pumping power. The main purpose of this behavior is the effects of longitudinal gradients at higher α. In general, the highest amount of pumping power occurs at α = 40° and 50° and for NF with φ = 4. The lowest pumping power is for the base fluid and at α = 20°. The lower depreciation of the fluid velocity on the rib with lower α is the reason for this behavior.

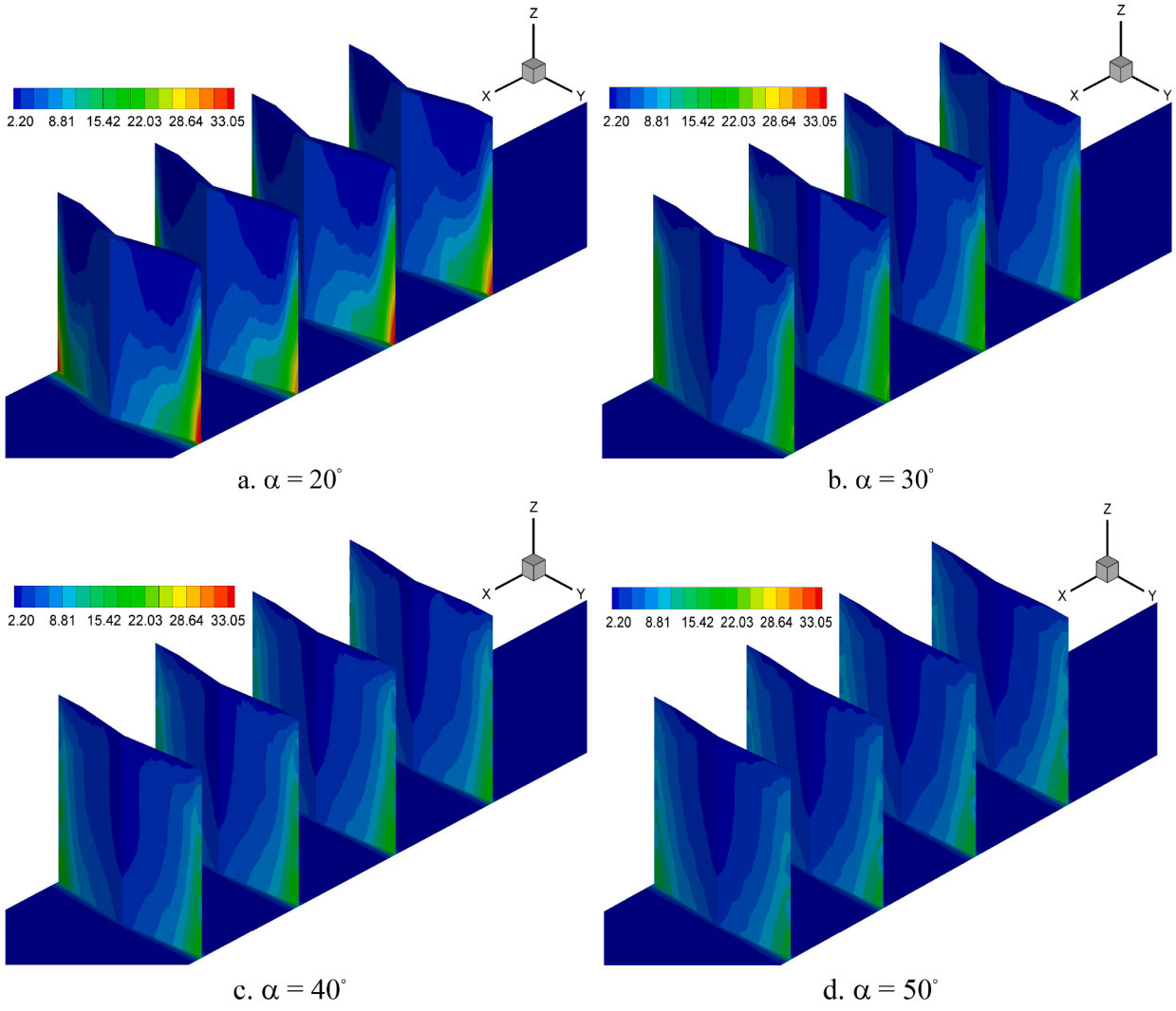

Fig. 19. Total entropy generation ($S_{gen,tot}$) contours at different α, φ = 0, and Re = 400.

5.6. Thermal-fluidic efficiency (PEC)

In Fig. 17, the changes of the thermal-fluidic efficiency parameter at α = 20° to 50°, different Re, and φ = 0.04 are compared with each other.

The thermal-fluidic efficiency parameter can express the predominance of the effect of increasing Nu or the friction factor due to the increase in φ and the increase in α in NF. In a ribbed channel, the use of NF can cause a significant increase in heat transfer, which was seen in the Nu_{ave} graphs. Moreover, with the increase of φ, the presence of frictional effects in the areas of the ribs and other walls of the microchannel was reported. According to Fig. 17, it can be seen that at Re = 1200, the increase of α increases the thermal efficiency parameter. At Re<1200, the highest thermal-fluidic efficiency is obtained by reducing α. The cause of this behavior was explained by interpreting Nu and f graphs; so, at α = 20°, the highest Nu and the lowest f are obtained. This behavior increases the thermal efficiency parameter of fluids.

5.7. Entropy generation (S_{gen})

Fig. 18 illustraites $S_{gen,tot}$ for α = 20° to 50° and φ = 0 to 0.04 and for Re = 1200-700. According to the diagrams, this factor is drawn based on the increase of heat penetration between fluid layers, and the increase of friction effects, and is proposed as $S_{gen,tot}$. Among the examined modes, the lowest amount of $S_{gen,tot}$ is related to α = 20°, the highest amount occurs at α = 40°. Increasing φ can also increase frictional S_{gen} and decrease heat transfer S_{gen}. The contrast between these two cases determines $S_{gen,tot}$.

The contours of Fig. 19 describe the behavior of $S_{gen,tot}$ in the ribbed hot region, at different attack angles, φ = 0, and Re = 400.

The entropy contours shown are related to S_{gen} due to the increase in heat transfer and the effects of temperature penetration in the fluid and the increase in entropy due to the friction effects. In all the contours, it can be seen that in the areas where the heat transfer rate is lower, S_{gen} has the highest value. At the Re = 400 and in the investigated attack angles, the case with α = 20° is affected by the hottest areas behind the rib. According to entropy contours, in these areas, the amount of generated entropy has the maximum value. By increasing φ, the penetration of fluid to the back of the ribs becomes possible; In these diagrams, the minimum amount of S_{gen} is for α = 40° and 50°. In general, the behavior of S_{gen} is the same as the growth of dimensionless temperature, and at Re = 400, the maximum amount of S_{gen} is related to α = 20°.

5.8. Dimensionless temperature variations

The graphs in Fig. 20 compare the local changes of the dimensionless temperature (θ) along the center line of the flow and for the Re = 400 in different φ and α = 20° to 50° of V-shaped ribs. As the cold fluid enters the microchannel and transfers heat between the fluid and the hot ribbed surface, heat penetration and the growth of the thermal boundary

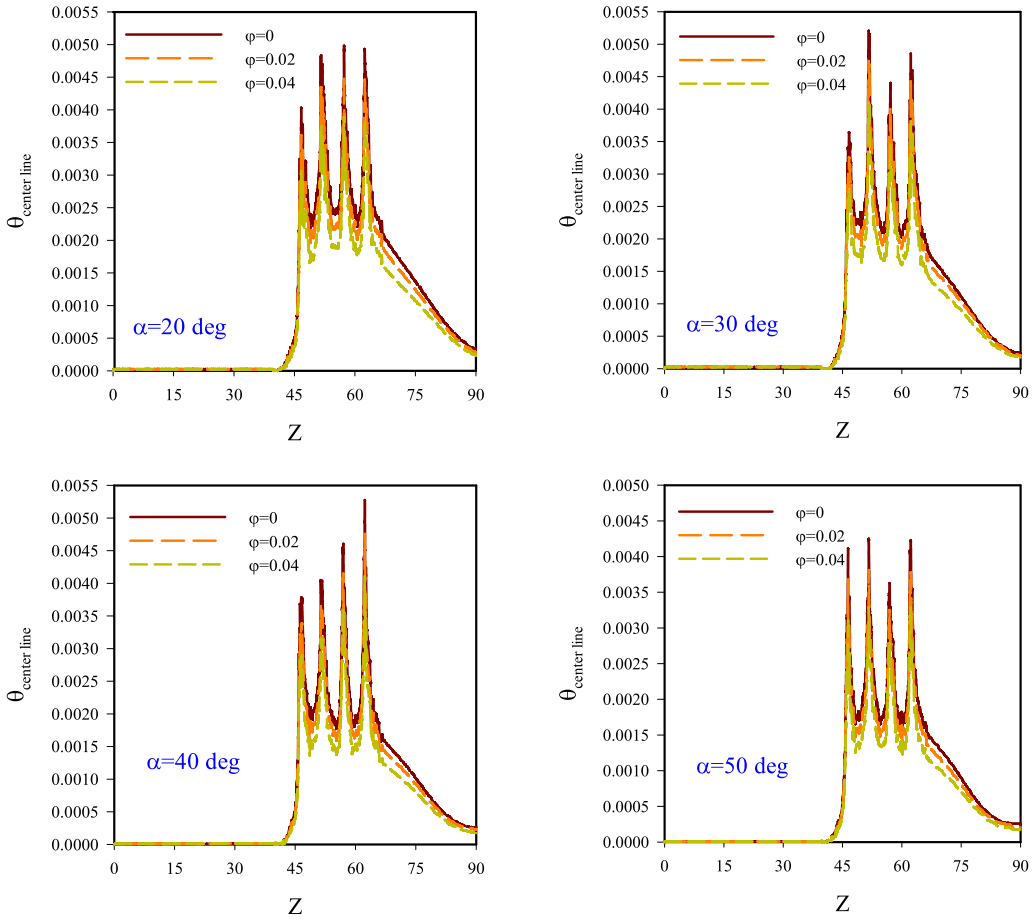

Fig. 20. Dimensionless temperature behavior in the centerline of the flow at Re = 400.

layer and its transfer to the central core areas of the flow increase. In the areas where the ribs are located and the wall is hot, the temperature gradients and the thermal boundary layer have the highest value and the highest growth. As the fluid moves between ribs, the thermal boundary layer is destroyed and re-formed.

This behavior also affects the local changes of θ. Therefore, it can be seen in all the graphs that the changes in θ are associated with certain fluctuations. After the fluid passes through the ribbed areas, because the end length of the microchannel is insulated and the heat transfer to the cooling fluid does not take place through the walls, the central temperature decreases. It can be seen in all the graphs that the effects of hot wall temperature penetration in the central core of the flow have the most penetration for the base fluid. The lowest hot temperature in the center line of the flow corresponds to NF with φ = 4.

6. Conclusions

Although many studies have been reported by researchers on the use of ribs and roughness in different geometries, the specific structure of the ribs in the microchannel and the presence of nanofluids using a two-phase mixture model distinguish the results of this study from other studies. In this research, V-shaped ribs with different attack angles were used on the bottom of the microchannel to increase the heat transfer efficiency. A nanofluid composed of water-aluminum oxide was used as the working fluid in the volume fractions of 0, 0.02 and 0.04 with Re = 400, 700, 1000, and 1200. The simulations were performed using FVM. The two-phase heat transfer of laminar flow in a 3D rectangular microchannel exposed to a constant heat flux of q" = 30000W/m^2 was analyzed and investigated. The results of this research show that the maximum velocity of the fluid is seen in the areas above the ribs. This behavior is caused by the narrowing of the lateral section of the channel. After the fluid passes over the ribs, with the increase of the attack angle (α), the velocity gradients have clear changes. The amount of changes in the local friction factor is dependent on the changes in the velocity gradients in the areas near the surfaces. In the pressure drop diagrams, because the fluid changes the velocity components by moving along the ribbed path, the pressure drop increases and the fluid momentum decreases. By increasing Re, the attack angle of ribs, and volume fraction, the pressure drop increases. But at low Re, because of the mentioned reasons, the amount of pressure drop will not have a special dependence on the increase in α and the increase in φ. The presence of a rib with a greater α causes stronger longitudinal vortices, and the presence of a rib with a lower α causes the creation of transverse vortices in the fluid flow. The highest amount of Nusselt number occurs at Re = 700 to 1200 at α = 20°. The behavior of increasing Nusselt number at Re = 400 is such that the highest amount of Nu corresponds to α = 30°, 40°, and 50°, and α = 20° degrees has the lowest value of Nu. Among the examined modes, the lowest amount of S_{gen} corresponds to α = 20° and the highest value corresponds to α = 40°, 30°, and 50°.

CRediT authorship contribution statement

Ali Koveiti: Conceptualization, Methodology, Software, Writing – original draft. **Ali B.M. Ali:** Conceptualization, Methodology, Software, Writing – original draft. **Sabah F.H. Alhamdi:** Validation, Formal analysis, Investigation, Writing – original draft. **Omid Ali Akbari:** Resources, Data curation, Writing – original draft, Writing – review & editing, Visualization, Supervision. **Gholamreza Ahmadi:** Resources,

Data curation, Writing – original draft, Writing – review & editing, Visualization, Supervision. **Soheil Salahshour:** Project administration, Funding acquisition, Writing – original draft. **Sh. Baghaei:** Project administration, Funding acquisition, Writing – original draft.

Declaration of competing interest

The authors declare that they have no known competing financial interests or personal relationships that could have appeared to influence the work reported in this paper.

Data availability

No data was used for the research described in the article.

References

[1] Guilian Wang, Zhichun Wang, Liyan Lai, Dongdong Xie, Yuan Zhu, Guifu Ding, Qiu Xu, Experimental and numerical investigation of hydrothermal performance of a microchannel heat sink with pin fins, Case Stud. Therm. Eng. 60 (2024) 104631.

[2] Guilian Wang, Kun Sheng, Yunran Wang, Guifu Ding, Dongdong Xie, Thermal hydraulic performance of tree-like microchannel heat sink with high branching level based on the improved Murray's law, Int. J. Heat Mass Transf. 231 (2024) 125875.

[3] M. Fiebig, Y. Chen, Heat transfer enhancement by wing-type longitudinal vortex generators and their application to finned oval tube Heat exchanger elements, in: S. Kakaç, A.E. Bergles, F. Mayinger, H. Yüncü (Eds.), Heat Transfer Enhancement of Heat Exchangers. Nato ASI Series, Heat Transfer Enhancement of Heat Exchangers. Nato ASI Series, 355, Springer, Dordrecht, 1999, https://doi.org/10.1007/978-94-015-9159-1_6.

[4] Mehdi Bahiraei, Nima Mazaheri, Hossein Moayedi, Employing V-shaped ribs and nanofluid as two passive methods to improve second law characteristics of flow within a square channel: A two-phase approach, Int. J. Heat Mass Transf. 151 (2020) 119419.

[5] Majid Kerdarian, Ehsan Kianpour, Flow field, heat transfer and entropy generation of nanofluid in a microchannel using the finite volume method, J. Comput. Appl. Res. Mech. Eng. 8 (2) (2018) 211–222, https://doi.org/10.22061/JCARME.2018.794.

[6] Sirine Chtourou, Hassene Djemel, Mohamed Kaffel, Mounir Baccar, Predicting the effect of the rib pitch on thermal performance factor of small channels plate heat exchangers fitted with Y and C shapes obstacles, SN Appl. Sci. 3 (2021) 497, https://doi.org/10.1007/s42452-021-04473-z.

[7] Haneen M. Al-Ali, Naseer H. Hamza, The effect of ribs spacing on heat transfer in rectangular channels under the effect of different types of heat flux in the presence of a nanofluids, AL-Qadisiyah J. Eng. Sci. 14 (2021) 095–103.

[8] Kourosh Javaherdeh, Habib Karimi, Numerical analysis of the obstacle effect with different geometry on the heat transfer of nanofluid flow in a rectangular channel, J. Appl. Comput. Sci. Mech. 35 (3) (2023) 51–64.

[9] E. Hosseinirad, M. Khoshvaght-Aliabadi, F. Hormozi, Effects of splitter shape on thermal-hydraulic characteristics of plate-pin-fin heat sink (PPFHS), Int. J. Heat Mass Transf. 143 (2019) 118586.

[10] M. Rezaee, M. Khoshvaght-Aliabadi, A.A. Abbasian Arani, S.H. Mazloumi, Heat transfer intensification in pin-fin heat sink by changing pin-length/longitudinal-pitch, Chem. Eng. Process.: Process Intensif. 141 (2019) 107544.

[11] B.H. Salman, H.A. Mohammed, K.M. Munisamy, A.Sh. Kherbeet, Characteristics of heat transfer and fluid flow in microtube and microchannel using conventional fluids and nanofluids, Renew. Sustain. Energy Rev. 28 (2013) 848–880.

[12] S. Mirmasoumi, A. Behzadmehr, Effect of nanoparticles mean diameter on mixed convection heat transfer of a nanofluid in a horizontal tube, Int. J. Heat Fluid Flow 29 (2008) 557–566.

[13] M. Akbari, A. Behzadmehr, F. Shahraki, Fully developed mixed convection in horizontal and inclined tubes with uniform heat flux using nanofluid, Int. J. Heat Fluid Flow 29 (2008) 545–556.

[14] M. Akbari, N. Galanis, A. Behzadmehr, Comparative assessment of single and two-phase models for numerical studies of nanofluid turbulent forced convection, Int. J. Heat Fluid Flow 37 (2012) 136–146.

[15] Mohamed A. Teamah, Mohamed M. Khairat Dawood, Ali Shehata, Numerical and experimental investigation of flow structure and behavior of nanofluids flow impingement on horizontal flat plate, Exp. Therm. Fluid Sci. 74 (2016) 235–246.

[16] Omid Ali Akbari, Arash Karimipour, Toghraie Davood, Mohammad Reza Safaei Semiromi, Habibollah Alipour, Marjan Goodarzi, Mahidzal Dahari, Investigation of rib's height effect on heat transfer and flow parameters of laminar water-Al2O3 nanofluid in a two dimensional rib-microchannel, Appl. Math. Comput. Appl. Math. Comput. 290 (2016) 135–153.

[17] M. Shariat, A. Akbarinia, A. Hossein Nezhad, A. Behzadmehr, R. Laur, Numerical study of two phase laminar mixed convection nanofluid in elliptic ducts, Appl. Therm. Eng. 31 (2011) 2348–2359.

[18] O. Ghaffari, A. Behzadmehr, H. Ajam, Turbulent mixed convection of a nanofluid in a horizontal curved tube using a two-phase approach, Int. Com- munic. Heat Mass Transf. 37 (10) (2010) 1551–1558.

[19] L. Schiller, A. Naumann, A drag coefficient correlation, Z. Ver Dtsch. Ing 77 (1935) 318.

[20] M. Manninen, et al., On the Mixture Model for Multiphase Flow, VTT Publications, Esppo, Finland, 1996.

[21] H. Chon, K.D. Kihm, S.P. Lee, S.U.S. Choi, Empirical correlation finding the role of temperature and particle size for nanofluid (Al2O3) thermal conductivity enhancement, Appl. Phys. Lett. 87 (2005) 1–3.

[22] J. Lee, I.J.I.J.o.H. Mudawar, M. Transfer, Assessment of the effectiveness of nanofluids for single-phase and two-phase heat transfer in micro-channels, Int. J. Heat Mass Transf. 50 (3-4) (2007) 452–463.

[23] K. Khanafer, K. Vafai, M. Lightstone, Buoyancy-driven heat transfer enhancement in a two dimensional enclosure utilizing nanofluids, Int. J. Heat Mass Transf. 46 (2003) 3639–3653.

[24] Prof. M.R. Safaei, M. Gooarzi, O.A. Akbari, M. Safdari Shadloo, M. Dahari, Performance evaluation of nanofluids in an inclined ribbed microchannel for electronic cooling applications, in: S M Sohel Murshed (Ed.), Electronics Cooling, InTech, 2016, https://doi.org/10.5772/62898. Prof.Available from, http://www.intechopen.com/books/electronics-cooling/performance-evaluation-of-nanofluids-in-an-inclined-ribbed-microchannel-for-electronic-cooling-appli.

[25] S. Aminossadati, A. Raisi, B.J.I.J.o.N.-L.M. Ghasemi, Effects of magnetic field on nanofluid forced convection in a partially heated microchannel, Int. J. Non Linear Mech. 46 (10) (2011) 1373–1382.

[26] R.L. Webb, Performance evaluation criteria for use of enhanced heat transfer surfaces in heat exchanger design, Int, J. Heat Mass Transf. 24 (1981) 715–726.

[27] O. Mahian, A. Kianifar, C. Kleinstreuer, A.-N. Moh'd A, I. Pop, A.Z. Sahin, S. Wongwises, A review of entropy generation in nanofluid flow, Int. J. Heat. Mass Transf. 65 (2013) 514–532.

[28] Lei Chai, Guodong Xia, Liang Wang, Mingzheng Zhou, Zhenzhen Cui, Heat transfer enhancement in microchannel heat sinks with periodic expansion–constriction cross-sections, Int. J. Heat Mass Transf. 62 (2013) 741–751.

[29] Amer Rasheed, Muhammad Shoaib Anwar, Numerical computations of fractional nonlinear Hartmann flow with revised heat flux model, Comput. Math. Appl. 76 (10) (2018) 2421–2433.

[30] Mumtaz Khan, Amer Rasheed, Muhammad Anwar, Numerical analysis of nonlinear time-fractional fluid models for simulating heat transport processes in porous medium, ZAMM - J. Appl. Math. Mech./Z. Angew. Math. Mech. 103 (2023), https://doi.org/10.1002/zamm.202200544.

[31] İhsan Dağtekin, Hakan F. Öztop, Ahmet Z. Şahin, An analysis of entropy generation through a circular duct with different shaped longitudinal fins for laminar flow, Int. J. Heat Mass Transf. 48 (1) (2005) 171–181.

[32] Fatih Selimefendigil, Hakan F. Öztop, Forced convection in a branching channel with partly elastic walls and inner L-shaped conductive obstacle under the influence of magnetic field, Int. J. Heat Mass Transf. 144 (2019) 118598.

[33] Igor V. Miroshnichenko, Mikhail A. Sheremet, Hakan F. Oztop, Nidal Abu-Hamdeh, natural convection of alumina-water nanofluid in an open cavity having multiple porous layers, Int. J. Heat Mass Transf. 125 (2018) 648–657.

[34] M. Irfan, M.S. Anwar, Abas Siti Sabariah, Muhammad Taseer, Hussain Zakir, Khan Mumtaz, Thermal behavior and efficiency enhancement of CuO - Al_2O_3 hybrid nanofluids using fractional calculus, J. Therm. Anal. Calorim. (2024), https://doi.org/10.1007/s10973-024-13822-0.

[35] Ali Haider, M.S. Anwar, Yufeng Nie, Fahad Saleh Almubaddel, Magda Abd El-Rahman, Optimizing heat and mass transfer in Carreau nanofluid with mixed nanoparticles in porous media using explicit finite difference method, Case Stud. Therm. Eng. 64 (2024) 105428.

[36] V. Puneeth, M.S. Anwar, M.R. Khan, Bioconvective Darcy–Frochherimer flow of the Ree–Eyring nanofluid through a stretching sheet with velocity and thermal slips, Waves Random Complex Media (2022) 1–22, https://doi.org/10.1080/17455030.2022.2157507.

[37] M.S. Anwar, Heat transfer in MHD convective stagnation point flow over a stretching surface with thermal radiations, Numer. Heat Transf. A: Appl. (2024) 1–16, https://doi.org/10.1080/10407782.2023.2299289.

[38] V. Puneeth, K. Sini, T. Clair, et al., Flow of nanofluid past a stretching cylinder subject to Thompson and Troian slip in the presence of gyrotactic microorganisms, Multiscale Multidiscip. Model. Exp. Des. 8 (2025) 84, https://doi.org/10.1007/s41939-024-00667-1.

[39] F. Sanei, et al., Numerical simulation of the nanofluid flow and heat transfer in porous microchannels with different flow path arrangements using single-phase and two-phase models, Int. J. Thermofluids 24 (100846) (2024) 100846, https://doi.org/10.1016/j.ijft.2024.100846.

[40] S. Hashemi Karouei, et al., On the thermal performance of a shell and double coil heat exchanger: numerical analysis of the geometrical characteristics impacts, Case Stud. Therm. Eng. 63 (105349) (2024) 105349, https://doi.org/10.1016/j.csite.2024.105349.

[41] Al-Asadi, et al., A computational analysis of the impact of nanofluids (Al2O3)on the PCM melting process in a rectangular container, Discov Sustain 5 (2024) 218, https://doi.org/10.1007/s43621-024-00429-6.

[42] B. Guo, et al., Numerical analysis of turbulent natural convection in the presence of wire-induced non-uniform magnetic field inside a porous medium, Int. Commun. Heat Mass Transf. 160 (108398) (2025) 108398, https://doi.org/10.1016/j.icheatmasstransfer.2024.108398.

[43] N. Ben Ali, K.A. Hammoodi, S. Aminian, A. Sharma, D.J. Jasim, A.I. Hameed, S. H. Hashemi, Analyzing heat transfer in a horizontal geothermal heat exchanger using numerical methods, Case Stud. Therm. Eng. 64 (105443) (2024) 105443, https://doi.org/10.1016/j.csite.2024.105443.